FOURTEENTH EUROPEAN ROTORCRAFT FORUM

Paper No. 21

A COUPLED ROTOR AEROELASTIC ANALYSIS UTILIZING NON-LINEAR AERODYNAMICS AND REFINED WAKE MODELLING

Michael S. Torok and Inderjit Chopra

Center for Rotorcraft Education and Research
Department of Aerospace Engineering
University of Maryland
College Park, MD 20742, U.S.A.

20-23 September, 1988
MILANO, ITALY

ASSOCIAZIONE INDUSTRIE AEROSPAZIALI
ASSOCIAZIONE ITALIANA DI AERONAUTICA ED ASTRONAUTICA

A Coupled Rotor Aeroelastic Analysis Utilizing Non-Linear Aerodynamics And Refined Wake Modelling[1]

Michael S. Torok[2] and Inderjit Chopra[3]

Center for Rotorcraft Education and Research
Department of Aerospace Engineering
University of Maryland
College Park, MD 20742, U.S.A.

1 ABSTRACT

The effects of improved aerodynamic modelling on rotor blade section and root loads, and blade response, are investigated. A non-linear aerodynamic model based on an indicial method, is incorporated into a coupled rotor aeroelastic analysis. The aerodynamic analysis consists of three phases: a linear attached flow solution, a separated flow solution, and a dynamic stall solution. A free wake model is also included into the analysis. Blade responses and loadings are calculated using a finite element formulation in space and time. A modified Newton iterative method is used to calculate blade response and trim controls as one coupled solution. Results show that at high speed flight conditions, non-linear effects dominate blade section forces, and significantly affect blade root loads. These effects are amplified at higher thrust conditions. Compressibility effects considerably influence the extent of separated flow on the rotor disk. Inclusion of the free wake analysis had only a limited effect on blade response and blade loads for a high speed flight condition.

2 INTRODUCTION

The modelling of aerodynamics for rotorcraft applications has undergone increased scrutiny in recent years due to the necessity to better predict the dynamic characteristics of rotorcraft. The past few years has seen the emergence of a multitude of highly complex CFD codes aimed at accurate predictions of rotary-wing aerodynamics [1,2]. The requirement of an aerodynamic model to be computationally "reasonable", in order to be implemented into a comprehensive aeroelastic

[1]Presented at the 14th European Rotorcraft Forum, Milano, Italy, September 20-23, 1988

[2]Rotorcraft Fellow

[3]Professor

analysis, however, precludes use of such codes. Technological advances in computing power continually expands this "reasonable" range, but significant improvements are still required. Thus, analysts are faced with the problem of balancing technological complexity, accuracy, and computational feasibility.

In the past five years, significant gains have been made in the methodologies of aerodynamic modelling. Several approaches have been undertaken. One approach is to capture the global unsteady effects on a rotor by use of a dynamic inflow model [3]. This method is limited to low frequency effects, and thus cannot predict detailed flow phenomena. This method was utilized in a dynamic analysis of a rotor in forward flight by Panda and Chopra [4]. In order to better define the aerodynamic complexities, several approaches concentrated on a blade-element analysis. Several theories, constrained by the assumption of harmonic motion, e.g. Loewy theory, and Greenberg theory, were generalized to arbitrary motions in References [5,6]. Recently, a finite state time-domain aerodynamic model was included in an aeroelastic stability and response analysis [7]. One limitation presents itself in these approaches, only incompressible, attached flow is considered. One other approach involved a synthesization of experimental data [8]. This method encompassed any and all physical features of a "real" flow, however, needed expensive prerequisite experimental testing, and a large number of empirical coefficients to be incorporated into a dynamic analysis. Additional methodologies are discussed in reference [9].

The approach taken in this investigation is the use of an unsteady aerodynamic model that overcomes the shortcomings of other models, yet remains of the same order in computational cost. The improvements involve accurate predictions of attached flow, as well as separated and dynamically stalled flow, consideration of compressibility effects, and need limited prerequisite information of airfoil characteristics. A model postulated and refined by Beddoes, [10], and Leishman and Beddoes, [11], utilizing an indicial response method has been validated over a wide range of conditions. The indicial response method involves the calculation of the lift and pitching moment response to a step change of airfoil angle of attack, and then sums the contributions of past arbitrary changes using Duhamel's principle of superposition. This method, thus captures the effects of the angle-of-attack time history. Compressibility effects are inherent in the model. The complete model requires only static airfoil data, and limited unsteady data. The parameters derived from the unsteady data, however, are not sensitive to airfoil shape, and thus need not be recalculated for all airfoils. The linear, attached flow phase of this model has been utilized in a dynamic analysis investigating higher harmonic control actuation power requirements [12]. This aerodynamic refinement showed a slight improvement over quasi-steady strip theory, in predicting 3P vertical hub shear on a 1/6 dynamically scaled Boeing CH-47D rotor model. A modified version of the complete non-linear model was also incorporated into a dynamic analysis, [13]. Although this analysis was restricted to a flap-only bending condition, significant non-linear effects were apparent at high speed, high thrust conditions.

The blade-element methodologies discussed to this point account for only shed wake effects. To complete the overall aerodynamic model, trailed wake effects must be considered. The combination of shed and trailed vorticity create a wake structure that significantly affects a rotor blades' aerodynamic environment. Early analyses simplified the wake model to a uniform inflow distribution. A first order improvement to this model is assuming a linear distribution of inflow, such as the Drees wake model [14]. Recent literature has emphasized the need for further refinements to improve correlations to an acceptable level. Current technology provides several models, from classical skewed helices to free wake calculations, and comparisons have been made on their respective ability to predict rotor inflow over a range of flight conditions. Two recent papers have made a comprehensive study on the validity of current wake models. Reference [15] examines five models; Scully's free wake in CAMRAD, UTRC's free wake, generalized wake, and classical skewed helix wake, and Beddoes model. Surprisingly, all showed only limited success. Discrepancies, in all the models, appeared in underpredicting the amount of rotor upwash on the disk at higher speeds, and in being able to predict the location of maximum downwash. Reference [16] investigated two models, (Scully and Sadler), at a low speed condition. Results showed a superiority of Scully's model, although it showed limitations in predicting the formation of the tip vortices in the rolling-up wake region. One other reference, [17], investigated several wake options within CAMRAD. At high speed, differences between a prescribed wake and the Scully free wake were insignificant. Both of these options greatly improved correlation over a uniform inflow distribution.

The present analysis utilizes the free wake model from CAMRAD [18]. Although it has shown discrepancies in predicting experimental data, it is among the current state-of-the-art models available. Incorporation of this model into our dynamic analysis has provided us several wake options. In conjunction with the blade-element model discussed earlier, the present aeroelastic analysis includes a highly sophisticated, yet computationally feasible aerodynamic prediction capability. The structural model is of comprable sophistication, thus creating an overall model with advanced prediction capabilities. The present study will investigate the influence of several key parameters on blade loadings and responses, and determine the significance of the refined aerodynamics. Future efforts should lead to a correlation study, to ultimately determine the validity of these refinements, as well as an investigation into blade stability characteristics and incorporation of still better wake models as they become available.

3 ROTOR ANALYSIS

The present investigation utilizes an analysis which solves the coupled, non-linear periodic equations of blade motion and six trim equilibrium equations. The analysis is based on a finite element approximation in both space and time. Each blade is assumed to be an elastic beam undergoing flap bending, lag bending, elastic twist and axial deflection. The blades are discretized into a number of beam elements, each having fifteen degrees of freedom. To reduce computational time, a large number of finite element equations are transformed to the modal space as a few normal mode equations (6–8 modes are normally used). The periodic, non-linear, response solution is determined by using a temporal finite element discretization. Fourth order Lagrangian shape functions are utilized within each time element. The finite element in time formulation is based on Hamilton's weak principle. Resulting normal mode equations are ultimately solved as a set of non-linear algebraic equations. The solution is obtained utilizing an iterative, modified Newton method [4,19].

Concurrent with the solution of the blade equations of motion, is the solution of the vehicle trim equations. The vehicle is trimmed on all axes for both force and moment equilibrium (6 equations). The modified Newton solution method allows the two solutions to be coupled to produce a unique solution that satisfies both blade and vehicle equilibrium equations. The force summation method is used to determine hub forces as a sum of inertial and aerodynamic loadings [20].

3.1 AERODYNAMIC MODEL

The aerodynamic modelling consists of two primary phases; a blade-element scheme, and a global wake scheme. The blade-element aerodynamic model is formulated to allow either quasi-steady strip theory, or unsteady two-dimensional aerodynamics. The unsteady aerodynamics consist of three parts, a linear attached flow solution, a separated flow solution, and a dynamic stall solution, based on the work of Leishman and Beddoes [11].

3.1.1 Attached Flow

The attached flow aerodynamics are calculated using an indicial response method, based on the principle of superposition [21]. The indicial response scheme determines the aerodynamic loadings due to a step change in the airfoil downwash at the three-quarter chord position. This indicial response is then convoluted over time using the Duhamel integral. The indicial response is idealized into contributions from both circulatory, and non-circulatory loadings. The circulatory lift component is given by,

$$L_C(s, M) = -\frac{1}{2}\rho c C_{l_\alpha}(M) u_T(s) \left[\phi_C(s, M) u_P(0) + \int_0^s \phi_C(s-\sigma, M) \frac{\partial u_P(\sigma)}{\partial \sigma} d\sigma \right] \quad (1)$$

where u_T is the chordwise velocity component, u_P is the downwash at three-quarter chord, and C_{l_α} is the 2-dimensional compressible lift curve slope. Circulatory lift is defined in "s-time", which is the distance the airfoil travels in semi-chords. This is transformed into "azimuthal time", i.e. a function of azimuthal angle, ψ. The circulatory indicial function, ϕ_C is expressed as,

$$\phi_C(s, M) = 1 - A_1 e^{-b_1(1-M^2)s} - A_2 e^{-b_2(1-M^2)s} \quad (2)$$

This function is similar to the classical Kussner function [22], and represents the lift deficiency due to shed vortices in the near wake.

The impulsive or non-circulatory lift is similarly expressed as,

$$L_I(s, M) = -\frac{1}{2}\rho c u_T(s) \left[\phi_I(s, M) u_P(0) + \int_0^s \phi_I(s-\sigma, M) \frac{\partial u_P(\sigma)}{\partial \sigma} d\sigma \right] \quad (3)$$

with the impulsive indicial function as

$$\phi_I(s, M) = \frac{4}{M} e^{-s/T'_\theta} \quad (4)$$

where T'_θ is a Mach dependent time constant [21]. This function is based on a time history of the non-circulatory loading due to pressure wave propagation, with an initial value computed from piston theory. The total lift is the sum of these two components.

$$L(s, M) = L_C(s, M) + L_I(s, M) \quad (5)$$

The implementation of equations (1) and (3) is carried out by expressing these equations in a discrete time form. Such a form is compatible with the finite element discretization solution. The lift equation becomes,

$$C_{N_n} = \frac{1}{2}\rho c u_T C_{l_\alpha}(M) \alpha_{E_n} + \frac{4T_\theta}{M}(\Delta\dot{\alpha}_n - D_n^{(1)}) + \frac{4T_q}{M}(\Delta\dot{q}_n - D_n^{(3)}) \quad (6)$$

with,

$$\alpha_E = -u_{P_n} - X_n - Y_n \quad (7)$$

where X_n and Y_n are lift deficiency functions which represent the deficiency in downwash due to unsteady effects, $D_n^{(1)}$ is a time history impulsive angle of attack function, and $D_n^{(3)}$ is a time history impulsive pitch rate function. T_θ and T_q are Mach dependent time constants. Complete details can be found in [10,11,21].

The unsteady pitching moment about the quarter chord is, similarly to lift, a sum of circulatory and non-circulatory loadings. Circulatory contributions derive from the offset of the circulatory lift from the quarter chord (x_{ac}), and the induced pitching moment effect associated with the pitch rate induced camber. Non-circulatory contributions are impulsive moments due to angle of attack changes and pitch rate. This yields,

$$C_M = \frac{-\pi}{8\beta}q_E + (\frac{1}{4} - x_{ac})C_N^C + C_{M_I}^{(1)}(\alpha_E, M, T_{\theta_M}) + C_{M_I}^{(2)}(q_E, M, T_{q_M}) \qquad (8)$$

where, q_E is an effective pitch rate, β is the Prandtl-Glauert correction factor, $C_{M_I}^{(1)}$ and $C_{M_I}^{(2)}$ are impulsive moment contributions due to angle of attack and pitch rate, respectively, and T_{θ_M} and T_{q_M} are Mach dependent time constants [21].

The unsteady drag can be derived from this lift force component, and the airfoil chordwise force [23]. The chordwise force arises from the component of lift in the chordwise direction, scaled by a leading edge suction efficiency factor (η_C).

$$C_T = \eta_C C_N \sin \alpha_E \qquad (9)$$

Due to the combination of decaying non-circulatory loading, and the build up of circulatory loading, the important result of a non-zero pressure drag under unsteady forcing conditions is obtained. Pressure drag tends to its static value in the limit of the unsteadiness decaying to zero. The total drag is the sum of this pressure drag and the airfoil viscous drag.

$$C_D = [C_N \sin \alpha - C_T \cos \alpha] + C_{D_0} \qquad (10)$$

These components are transformed into a discrete time form with appropriate time history functions and time constants. These three components, lift, drag, and pitching moment are incorporated into the analysis scheme and determine the unsteady attached flow solution.

3.1.2 Separated Flow

The second phase of the unsteady blade-element aerodynamic model involves corrections to the attached flow solution due to flow separation. A method, based on Kirchhoff theory, has been implemented [10]. Kirchhoff theory relates the normal force coefficient in terms of the trailing edge separation point, f.

$$C_N = C_{l_\alpha}(M)\left[\frac{1+\sqrt{f}}{2}\right]^2 \alpha \tag{11}$$

Thus, if the separation point is known, it is easy to determine the normal force. Accordingly, if the normal force and angle of attack are known from experiment, the separation point behavior can be implied. This, however, is a static result, and must be modified to represent unsteady conditions. Two physical phenomena have been identified that affect separation point behavior [10]. The first is a lag associated with the leading edge pressure response, beyond the normal force lag associated with unsteady forcing conditions. The second is the effects of the unsteady boundary layer. Thus, the methodology is as follows; calculate a pressure lagged, "effective" angle of attack, and use this value in the static airfoil separation point relation to obtain a lagged separation point. The final step is to apply a boundary layer lag to obtain the unsteady separation point. This value is inserted into the Kirchhoff relation, equation (11), to obtain the unsteady separated flow normal force.

The calculation of a separated flow chord force, and thus a drag force, equation (10), is deduced from Kirchhoff theory, i.e.,

$$C_T = \eta_C C_{l_\alpha}(M)\sqrt{f}\alpha^2 \tag{12}$$

Further details are given in reference [11].

The final part of the separated flow solution involves determination of pitching moment characteristics due to flow separation. Kirchhoff theory has no general expression for pitching moment behavior. Thus, an empirical curve fit must be utilized to represent the variation of airfoil center of pressure, as a function of separation point,

$$\frac{C_M}{C_N} = K_0 + K_1(1-f) + K_2\sin(\pi f^2) \tag{13}$$

where, K_0, K_1, and K_2, are empirical parameters, obtained from static data. This result, rearranged, gives the separated pitching moment behavior. These three parts sum to yield the separated flow solution.

3.1.3 Dynamic Stall

The third and final phase of the unsteady blade-element aerodynamic model is a semi-empirical method for dynamic stall. Several physical phenomena must be modelled to accurately represent the aerodynamic loadings on the airfoil: the magnitude of the vortex induced lift, the conditions upon which it separates from the leading edge, and the time history of the vortex as it traverses the chord and dissipates into the wake. Investigation into experimental data [11] shows that an acceptable model relates the excess vortex lift to the difference between the attached flow lift and the separated flow lift contribution. This excess lift is allowed to decay exponentially, while simultaneously being incremented at each step. Numerically, this can be represented as,

$$C_V = C_N^C \left[1 - \left(\frac{1+\sqrt{f}}{2}\right)^2\right] \tag{14}$$

$$C_{N_{V_n}} = F(C_{N_{V_{n-1}}}, C_{V_n}, C_{V_{n-1}}) \tag{15}$$

where, C_V is termed the excess lift due to the vortex, and C_{N_V} is the corresponding incremental value of lift due to the entire time history effect of the dynamic stall. The criteria upon which the vortex will separate from the leading edge is a function of the leading edge pressure gradient and the airfoil characteristics. A leading edge pressure parameter is calculated based on the pressure lag behind the airfoil normal force, C_n'. For every airfoil, a limit value of this parameter can be determined, C_n^1. The onset of vortex separation at the leading edge is indicated when C_n' exceeds C_n^1. The final effect that needs to be modelled is the rate of vortex travel across the chord. This rate has been shown experimentally to be approximately half of the free stream velocity [11]. This rate is also Mach dependent. As the vortex reaches the airfoil trailing edge and passes into the wake, its effect on the airloads is quickly reduced. Monitoring of the magnitude of the vortex induced lift, and its duration on the airfoil chord, yields an accurate representation of the airfoil lift characteristics under dynamically stalled conditions.

As a direct result of this dynamic stall process, the pitching moment characteristics of the airfoil are also changed. This variation is effectively modelled by representing the variation of the airfoil center of pressure, aft of the quarter-chord, as,

$$CP_V = \frac{1}{4}\left[1 + \sin\left\{\pi\left(\frac{\tau_V}{T_{VL}} - 0.5\right)\right\}\right] \tag{16}$$

where, τ_V is the non-dimensional time after the shedding of the vortex, and T_{VL} is the total time for the vortex to traverse the chord. The incremental pitching moment is then simply the vortex induced lift times the offset of the center of pressure from the quarter-chord position, i.e.,

$$C_{M_V} = -CP_V\, C_{N_V} \tag{17}$$

A number of modifications to the model are conducted to account for "interactional" effects among the individual elements of the model. These modifications are principally carried out through modifying just two time constants, one each associated with trailing edge separation, and vortex lift. These changes include the effects of separation suppression due to moderate pitch rates, and the acceleration of trailing edge separation due to either vortex separation at the leading edge or a change in pitch direction during vortex travel down the airfoil chord. Reattachment is also modelled by monitoring the leading edge pressure, C_n'', and adjusting the rate of reattachment depending on its value, (reattachment is initiated when C_n'' becomes less than C_n^1), as well as the location of any vortices in the flow. Appropriate logic for these phenomena is incorporated into the algorithm [11]. These modifications, in conjunction with the three phase blade-element unsteady aerodynamic model, result in a complete, non-linear aerodynamic model. It is important to note that this solution needs only minimal prerequisite information about the airfoil being modelled, is an efficient and accurate procedure, and can be formulated in a form compatible with a temporal finite element solution.

3.2 IMPLEMENTATION INTO ROTOR ANALYSIS

As mentioned earlier, the formulation of the aerodynamic model is compatible with the finite element in time solution technique. The discrete time algorithm "steps" through each temporal Gaussian integration point around the azimuth. Time-history effects are maintained by saving previous step information. The temporal finite element solution requires the response solution to be periodic. Consequently, the aerodynamics must also attain periodic time histories. Satisfaction of periodicity, as well as trim conditions, determine the final converged solution.

3.3 ROTOR WAKE ANALYSIS

The wake model refinements included in this rotor analysis include a linear (Drees) inflow model [14], and a free wake (Scully, Johnson) model [24,25]. The geometry of the free wake model is divided into three regions; near wake, rolling-up wake, and far wake. The near wake consists of a series of radial panels, each with linear circulation distributions. The rolling-up wake consists of an inboard linear circulation distribution panel, and a tip panel that represents the rolling up of the tip vortex. The far wake is simply one panel of linear circulation distribution, and a concentrated tip vortex, of strength proportional to the maximum circulation value on the rotor blade [18]. See Figure 1. The inboard vorticity is far less significant than the tip vortices due to a small circulation gradient inboard on the blade. Thus, a more approximate model can be used. Conversely, the tip vortex requires a refined model, i.e. a free wake model, to yield accurate results. The model used in this analysis prescribes the inboard wake with large core radii vortices, and allows the tip vortex geometry to vary. Vortex filaments with linear vorticity distributions are used. The extent of each region of the wake can be prescribed [18]. See Figure 2.

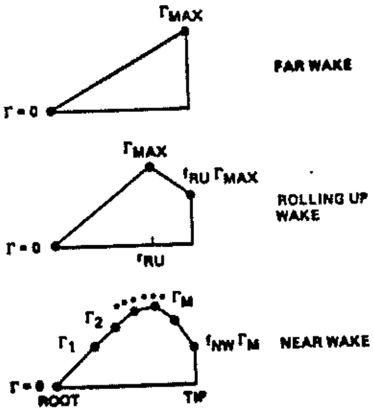

Figure 1.

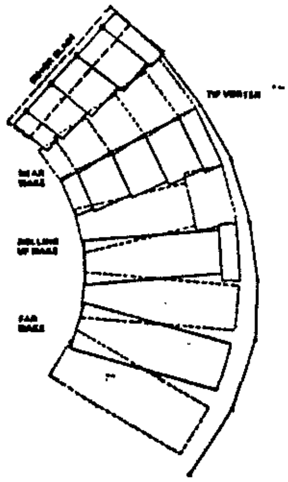

Figure 2.

The present analysis concentrates on the high speed flight regime. At such a condition, the problems of blade-vortex interactions are limited, and are commonly found on the "sides" of the rotor disk. Several modifications are utilized at these locations. First, the azimuthal step size is reduced, and secondly, since lifting line theory cannot represent the effects of chordwise variations in inflow, a lifting surface correction is used. One final modification was driven by experimental results showing a decreased influence of the vortex after such an interaction. A method of letting the vortex core "burst" or increase in radius after an interaction effectively models this phenomena, though the actual mechanics of the process are not fully understood [24]. Since shed wake effects are represented in the blade-element modelling, they are not accounted for in the wake model. For more details on the wake model, see [18,24,25].

4 RESULTS

The baseline rotor configuration is a four bladed hingeless rotor with fundamental rotating frequencies of flap, 1.13, lag, 0.70, and torsion, 4.47 per/rev. The flight condition is a high advance ratio, $\mu = 0.35$, with a hover tip Mach number of 0.7. The thrust coefficient over solidity, $C_T/\sigma = 0.07$. Baseline wake model attributes include a tip vortex core size of $.03R$, and four radial inflow calculation points, with the outermost point located at $X = 0.92R$. The rotor blade airfoil is a NACA 0012 section. The rotor blade aspect ratio is, radius/chord = 18. Additional rotor information is given in Table 1. A parametric study is undertaken to investigate the influence of linear unsteady aerodynamics, non-linear unsteady aerodynamics, thrust, Mach number, tip vortex size, and radial inflow point location. Comparisons are made between the Drees wake model, and the free wake model.

NOTE: In the figures, for blade response and root loads, the linear solution is the attached flow solution, and the non-linear solution is the complete model, including separation and dynamic stall. All results are using Drees wake, except where noted. The blade section results compare the linear unsteady solution, the non-linear solution, without dynamic stall, i.e. just separation effects, and the complete model, including dynamic stall. In the figures involving separation point, a value of 1, means no separation, i.e. the separation point is at the trailing edge. More and more separation exists as the value decreases toward zero, at the leading edge of the airfoil.

4.1 Baseline Case - Drees Wake Model

The baseline results are a comparison among, quasi-steady, linear (attached) unsteady, and non-linear (separation and dynamic stall) unsteady aerodynamics. Figures 3,4 and 5 show the blade tip response for flap, lag, and torsion respectively. Flap motion is primarily 2/rev, while lag and torsion are 1/rev motions. Non-linear effects result in a phase shift in flap response, and increased higher harmonic content, especially in the torsional retreating side response. The corresponding blade root vertical shear and flap bending moment, Figures 6,7, show amplified phase effects, as well as an increase in vertical shear oscillatory amplitudes on the retreating side. Examining the aerodynamic normal force and pitching moment at the tip, Figures 8,9 respectively, depict the flow being dominated by separation effects, with only limited dynamic stall. The separation is most evident on the advancing side, near the tip, while inboard, the flow remains attached, Figure 10.

4.2 Baseline Case - Free Wake Model

Inclusion of the free wake analysis at this flight condition yields only small changes in the results. Figures 11,12 show the variation in blade tip response magnitudes. Blade section aerodynamic forces are only slightly changed, see Figures 13,14, as compared to Figures 8,9 respectively. Similarly, blade root loads also show only small changes, Figures 15,16. It should be noted that results are also obtained for a prescribed wake geometry, based on Landgrebe's model for maximum circulation [26]. Discrepancies between the prescribed and free wake models are insignificant, concurring with Reference [17], thus prescribed wake results are not shown.

4.3 Compressibility Effects

To determine compressibility effects, the flight condition is changed to a tip Mach number of 0.55. A free wake analysis is used for these results. Results show that the separation effects, which dominated the flow at the tip region in the baseline case, are significantly reduced, Figures 17,18 as compared to Figures 13,14. At the reduced tip Mach number, blade response shows a reduction in lag response magnitude, Figure 19, and torsional oscillations, Figure 20. Flap response is primarily unaffected, and therefore not presented. Blade loads also exhibit reduced oscillatory amplitudes, Figures 21,22.

4.4 Tip Vortex Core Size and Inflow Point Location

Tip vortex core size, and the location of points at which the free wake inflow is calculated, are varied to determine their sensitivity on rotor loadings. First the four inflow calculation point locations were varied, the outermost point varying from $0.88R \leq X \leq 0.96R$. For each case, the tip vortex core size was varied from, $0.00275R \leq r_{CORE} \leq 0.03R$. None of these cases showed any significant effects. If the outermost inflow point is moved to the tip, ($X = 0.99R$), near the vortex core, however, results are significantly altered. The following results are for a modified tip vortex core size of 0.00275R, (5% chord), with the outermost inflow calculation point at $X = 0.99R$. Figures 23,24 present section normal force and pitching moment results, respectively. These figures show increased separation on the retreating side, plus a small region of dynamic stall at $\psi = 260\,\text{deg}$, as compared to the baseline case, Figures 13,14. Blade flap response magnitude is decreased, Figure 25, and torsional response magnitude is increased with decreased oscillations, Figure 26. Blade root loadings are also altered, particularly an increased peak-to-peak vertical shear, Figures 27,28. Therefore, judgement is required in the selection of the tip vortex core size, and inflow point locations, in order to attain accurate results.

4.5 Increased Rotor Thrust

In order to magnify the non-linear aerodynamic effects, the baseline flight condition is changed to a higher thrust coefficient, (from $c_T/\sigma = .07$ to $c_T/\sigma = .10$). As expected, the overall magnitudes in response and loadings are increased. More interesting, though, is the amplification of both separation and dynamic stall effects. At the tip, there is large separation effects around the entire azimuth, as opposed to just the advancing side in the baseline case, Figure 29, as compared to Figure 8. Vortex lift contributions to the total blade normal force are increased. In the tip section pitching moment plot, Figure 30, three regions of dynamic stall are apparent, two lesser stall regions, $\psi = 215$ deg, and $\psi = 310$ deg, and a large stall region at $\psi = 260$ deg. Inboard on the blade, the dynamic stall regions are at different azimuthal locations, $\psi = 220$ deg, and $\psi = 290$ deg, Figures 31,32. Figure 33 shows that the separated flow region is spreading inboard. Blade responses, see Figures 34,35 and 36, show a corresponding increase in non-linear effects, including phase shifts and increased higher harmonic content, as well as an increased lag response magnitude. Blade root loads also show substantial non-linear effects, Figures 37,38.

5 DISCUSSION

The inclusion of linear and non-linear unsteady aerodynamics has yielded a spectrum of interesting results. For all flight conditions investigated, the differences between quasi-steady and linear unsteady aerodynamic models are small. Small phase shifts and response attenuations are apparent. Non-linear effects are of more significance. The baseline, high speed, low thrust, flight condition yields results dominated by flow separation effects. These effects are concentrated at the blade tip, and are greater on the advancing side of the rotor disk. The NACA 0012 airfoil, at the high tip Mach numbers associated with this flight condition, (as high as M = 0.945 on the advancing side), stalls at very low angles of attack resulting in large amounts of separation. Reducing the hover tip Mach number from 0.7 to 0.55, equivalent to reducing tip speed from 770 ft/sec to 600 ft/sec, limits the maximum Mach number to M = 0.74 on the advancing side. This all but eliminates flow separation everywhere on the disk.

Increasing the thrust level, from $c_T/\sigma = .07$ to .10, greatly amplifies the effects of the non-linear aerodynamics. At the blade element level, two effects are apparent. One, the region of flow separation has spread to all azimuthal locations of the rotor disk, as well as spreading inboard from the tip. Secondly, regions of large dynamic stall exist on the retreating side of the disk. These regions appear at different azimuthal stations, for different radial locations. These two effects combine to cause increased higher harmonic content and phase shifts of the blade root loadings.

The free wake model implemented contains many parameters that govern wake geometry and distortion. To determine acceptable parameters, a correlation is carried out with results in Reference [27]. All values are then held constant throughout this investigation, except tip vortex core size, and the radial location of inflow calculation points. The baseline configuration utilizes the values of these two parameters, determined from Reference [27], and the correlation study. Results show that for the baseline flight condition, inclusion of the free wake analysis yields only small changes in blade response suggesting that the disk inflow has been slightly redistributed. Location of the inflow calculation points at the blade tip, near the vortex core, however, showed significant effects. Large changes in blade response magnitudes suggest a change in the mean inflow value over the disk. This also leads to different peak-to-peak shear loads. To determine the significance of these changes, a correlation study with flight test data is required.

An important factor which changes as a result of these parametric variations is the vehicle trim controls. These values are given in Table 2. Several interesting results are noticed. Non-linear aerodynamics required a much higher collective control input over linear or quasi-steady aerodynamics for all cases. The reduced tip Mach number case showed little change in controls. The baseline free wake case required reduced magnitudes of collective and cyclic controls, yet the modified tip vortex and inflow point case required increased magnitudes of collective and longitudinal cyclic control, and a decreased lateral cyclic control. The increased thrust case, as would be expected, required larger control inputs.

6 CONCLUSIONS

The following conclusions are drawn from this investigation:

1. A non-linear aerodynamic model has been successfully incorporated into a coupled rotor aeroelastic analysis.

2. Incorporation of new wake model options, including a free wake model, has also been completed successfully.

3. At high speed conditions, non-linear aerodynamic effects dominate out-

board blade section forces, and significantly affect blade response and blade root loads. These effects are amplified at increased thrust levels.

4. Compressibility effects significantly affect the extent of separated flow on the rotor blade.

5. For the baseline configuration, prescribed and free wake models give similar results to the Drees wake model.

6. Free wake modelling is insensitive to tip vortex core size when inflow calculation points are located away from the blade tip. Varying tip vortex core size, with an inflow point located at the blade tip, however, substantially modifies the mean inflow on the rotor disk.

7. Trim controls are affected by these parametric variations and must be considered as a factor in these results.

Acknowledgements

The authors acknowledge Dr. J.G. Leishman and Mr. Khanh Nguyen, of the University of Maryland, for their assistance throughout this effort. This research work was supported by the Army Research Office, Contract No. DAAL-03-88-C-0002; Technical Monitor, Dr. Robert Singleton.

References

[1] Caradonna,F.X., Tung,C., "A Review of Current Finite Difference Rotor Flow Methods", Presented at the 42nd Annual Forum of the American Helicopter Society, Washington D.C., June 1986.

[2] McCrosky,W.J., "Some Rotorcraft Applications of Computational Fluid Dynamics", Presented at the 2nd International Conference on Rotorcraft Basic Research, University of Maryland, Feb. 1988.

[3] Gaonkar,G.H., and Peters,D.A., "Effectiveness of Current Dynamic Inflow Models in Hover and Forward Flight", Journal of the American Helicopter Society, 31, No. 2, April 1986.

[4] Panda,B., Chopra,I., "Flap-Lag-Torsion Stability in Forward Flight", Journal of the American Helicopter Society, 30, No. 4, Oct. 1985.

[5] Dinyaveri and Friedmann, "Application of Time-Domain Unsteady Aerodynamics to Rotary-Wing Aeroelasticity", Presented at the Structures, Structural Dynamics, and Materials Conference, Orlando, Florida, April 1985.

[6] Friedmann, "Arbitrary Motion Unsteady Aerodynamics and its Application to Rotary-Wing Aeroelasticity", Journal of Fluids and Structures, 1, Jan. 1987.

[7] Friedmann and Robinson, "Influence of Time-Domain Unsteady Aerodynamics on Coupled Flap-Lag-Torsional Aeroelastic Stability and Response of Rotor Blades", Presented at the 2nd International Conference on Rotorcraft Basic Research, University of Maryland, Feb. 1988.

[8] Gangwani, "Synthesized Airfoil Data Method for Prediction of Dynamic Stall and Unsteady Airloads", Vertica 8, 1984.

[9] Friedmann, "Recent Trends in Rotary-Wing Aeroelasticity", Vertica 11, 1987.

[10] Beddoes,T.S., "Representation of Airfoil Behavior", Vertica 7, 1983.

[11] Leishman,J.G., Beddoes,T.S., A Generalized Model for Unsteady Aerodynamic Behavior and Dynamic Stall using the Indicial Method", Presented at the 42nd Annual Forum of the American Helicopter Society, Washington D.C., June 1986.

[12] Nguyen,K., Chopra,I., "Actuator Power Requirements for Higher Harmonic Control (HHC) Systems", Presented at the 2nd International Conference on Rotorcraft Basic Research, University of Maryland, Feb. 1988.

[13] Elliott,A.S., Leishman,J.G., Chopra,I., "Rotorcraft Aeromechanical Analysis Using a Non-Linear Unsteady Aerodynamic Model", Presented at the 44th Annual Forum of the American Helicopter Society, Washington D.C., June 1988.

[14] Drees,J.M., "A Theory of Airflow Through Rotors and its Application to Some Helicopter Problems", Journal of the Helicopter Association of Great Britain, Vol. 3, No. 2, July-September 1949.

[15] Hoad,D., Althoff,S., Elliott,J., "Rotor Inflow Variability with Advance Ratio", Presented at the 44th Annual Forum of the American Helicopter Society, Washington D.C., June 1988.

[16] Charles,B., Hassan,A., "A Correlation Study of Rotor Inflow in Forward Flight", Presented at the 44th Annual Forum of the American Helicopter Society, Washington D.C., June 1988.

[17] Yamauchi,G.K., Heffernan,R., Gaubert,M., "Correlation of SA349/2 Helicopter Flight Test Data with a Comprehensive Rotorcraft Model", Journal of the American Helicopter Society, 33, No. 2, April 1988.

[18] Johnson,W., "A Comprehensive Analytical Model of Rotorcraft Aerodynamics and Dynamics, Part 1: Analysis Development", NASA TM 81182, June 1980.

[19] Lim,J., Chopra,I., "Design Sensitivity Analysis for an Aeroelastic Optimization of a Helicopter Blade", Presented at the AIAA Dynamics Specialists Conference, Monterrey, California, April 1987.

[20] Lim,J., Chopra,I., "Aeroelastic Optimization of a Helicopter Rotor", Presented at the 44th Annual Forum of the American Helicopter Society, Washington D.C., June 1988.

[21] Leishman,J.G., "Validation of Approximate Indicial Aerodynamic Functions", Journal of Aircraft, Nov. 1988.

[22] Bisplinghoff,R.L., Ashley,H., Halfman,R.L., *Aeroelasticity*, Addison-Wesley Publishers, 1955.

[23] Leishman,J.G., "An Analytical Model for Unsteady Drag", Journal of Aircraft, July 1988.

[24] Scully,M.P., "Computation of Helicopter Rotor Wake Geometry and its Influence on Rotor Harmonic Airloads", Massachusetts Institute of Technology, ASRL TR 178-1, March 1975.

[25] Johnson,W., *Helicopter Theory*, Princeton University Press, 1980.

[26] Landgrebe,A.J., "The Wake Geometry of a Hovering Helicopter Rotor and its Influence on Rotor Performance", Journal of the American Helicopter Society, Vol. 17, No. 1, January 1977.

[27] Johnson,W., "Comparison of Calculated and Measured Helicopter Rotor Lateral Flapping Angles", Journal of the American Helicopter Society, 26, No. 2, April 1981.

$EI_y/m_0\Omega^2R^4$	$=$ 0.01080
$EI_z/m_0\Omega^2R^4$	$=$ 0.02680
$GJ/m_0\Omega^2R^4$	$=$ 0.00615
k_A/R	$=$ 0.02900
k_{m1}/R	$=$ 0.01320
k_{m2}/R	$=$ 0.02470

Table 1. Rotor Blade Uniform Structural Properties

		α_S	ϕ_S	θ_0	θ_{1C}	θ_{1S}	$\theta_{0_{tail}}$
Baseline DreesWake $M_{TIP} = 0.70$ $C_T/\sigma = .07$	*Quasi − Steady*	.128	−.037	.167	.046	−.105	.013
	Unsteady(lin)	.122	−.042	.167	.041	−.107	.014
	Unsteady(non − lin)	.128	−.046	.170	.042	−.101	.014
Baseline FreeWake $M_{TIP} = 0.70$ $C_T/\sigma = .07$	*Quasi − Steady*	.130	−.034	.156	.044	−.097	.012
	Unsteady(lin)	.121	−.034	.154	.041	−.102	.012
	Unsteady(non − lin)	.131	−.041	.159	.041	−.093	.013
ReducedM$_{TIP}$ *FreeWake* $M_{TIP} = 0.55$ $C_T/\sigma = .07$	*Unsteady(non − lin)*	.124	−.036	.159	.039	−.096	.012
IncreasedC$_T$ *DreesWake* $M_{TIP} = 0.70$ $C_T/\sigma = .10$	*Quasi − Steady*	.087	−.016	.178	.059	−.127	.015
	Unsteady(lin)	.083	−.021	.179	.051	−.130	.015
	Unsteady(non − lin)	.067	−.036	.216	.085	−.155	.028
ModifiedCore FreeWake $M_{TIP} = 0.70$ $C_T/\sigma = .07$	*Unsteady(non − lin)*	.120	−.051	.191	.030	−.119	.016

Table 2. Rotor Coupled Trim Controls

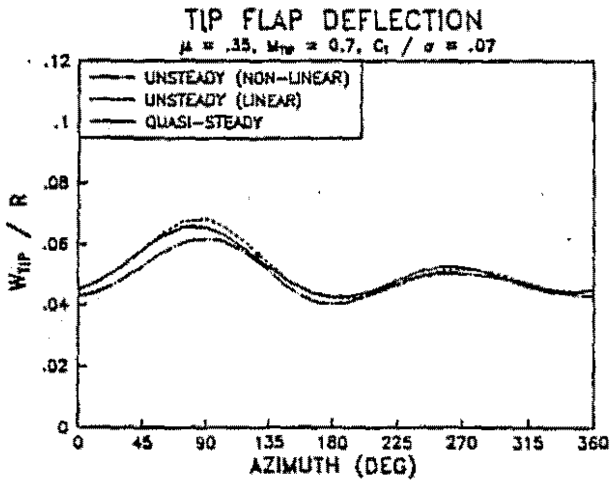

FIGURE 3.

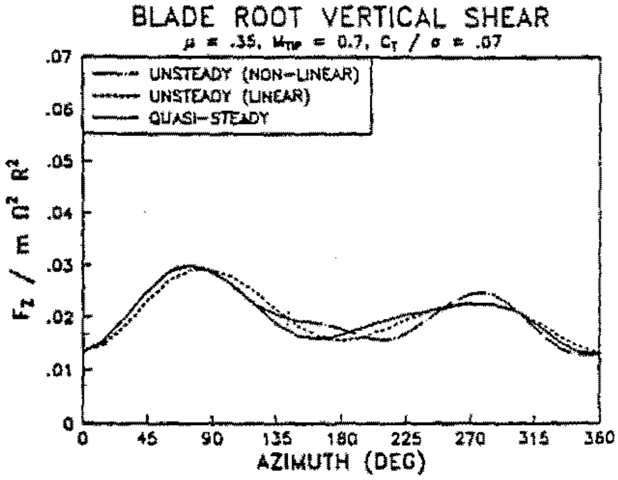

FIGURE 6.

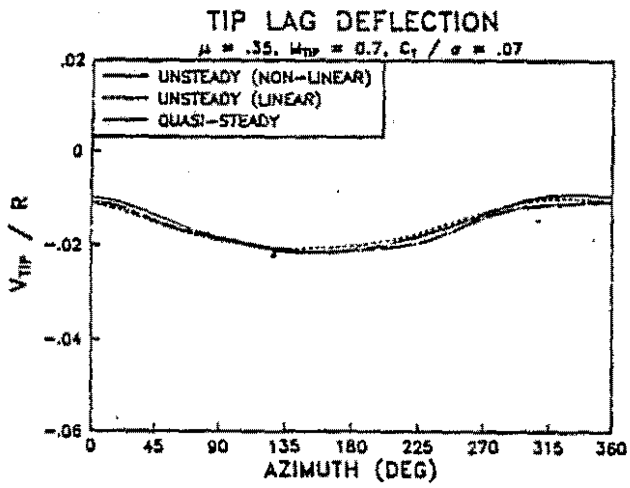

FIGURE 4.

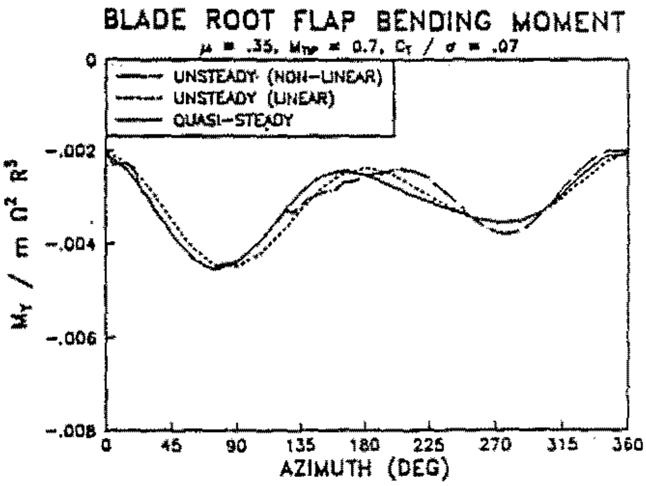

FIGURE 7.

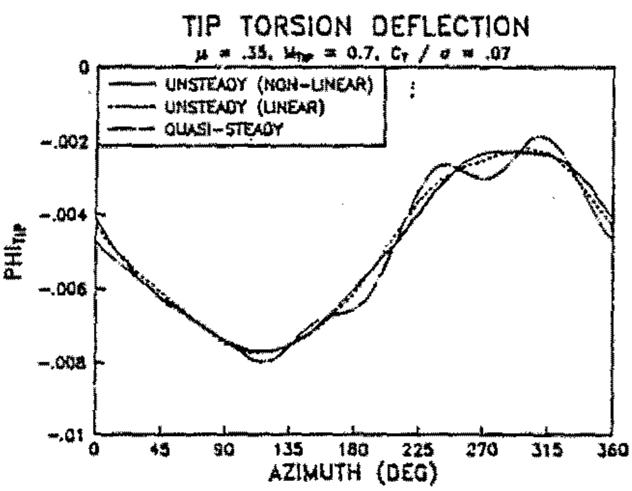

FIGURE 5.

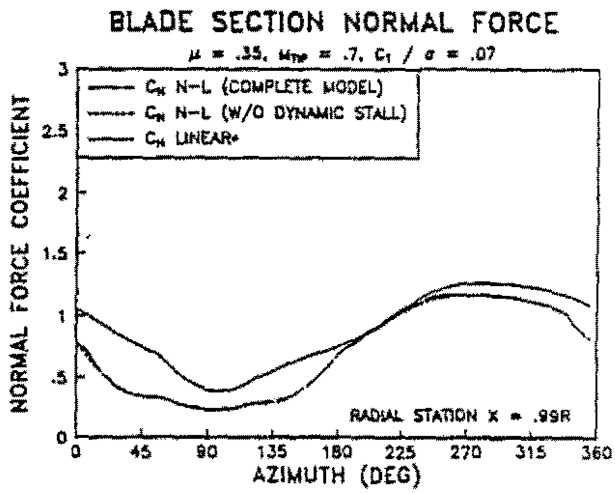

FIGURE 8.

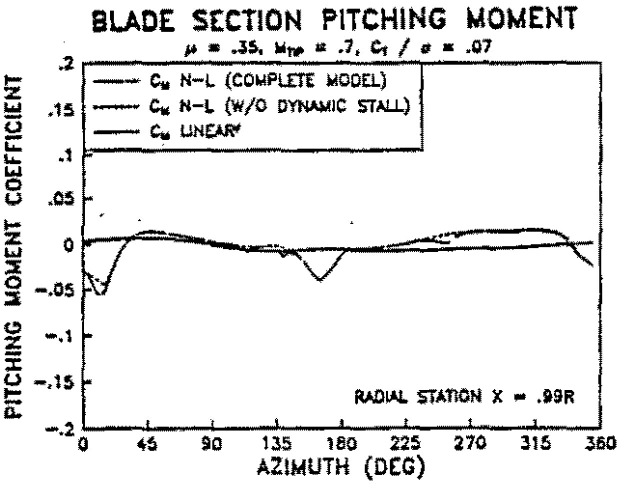

FIGURE 9.

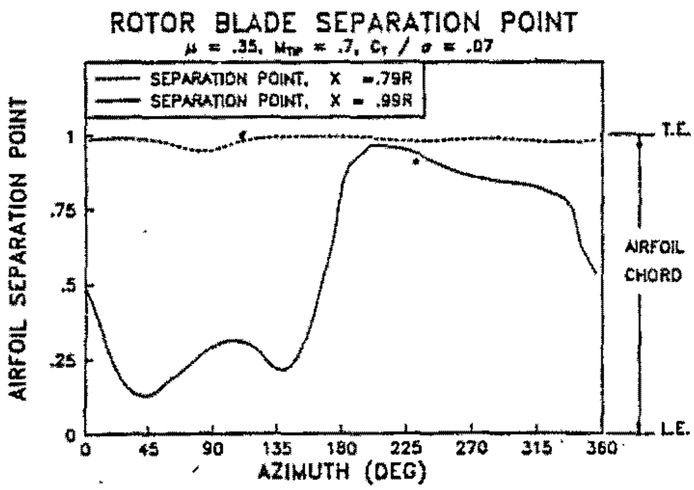

FIGURE 10.

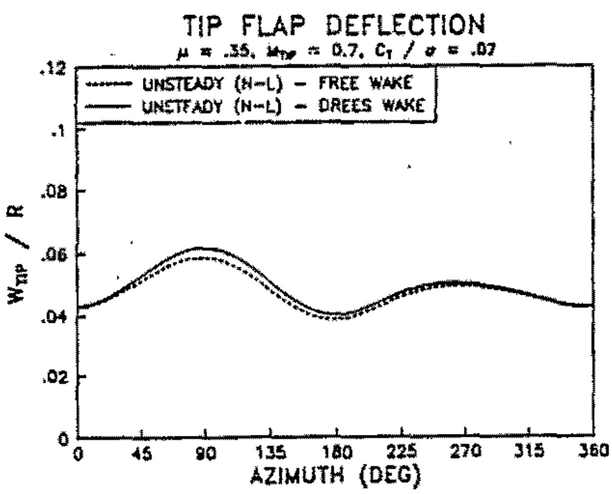

FIGURE 11.

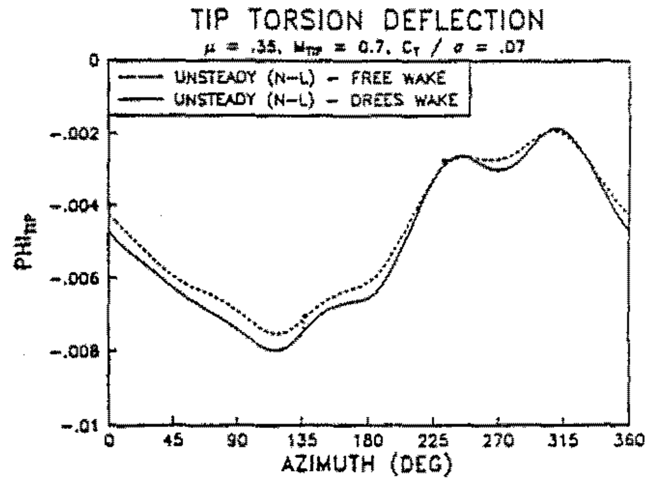

FIGURE 12.

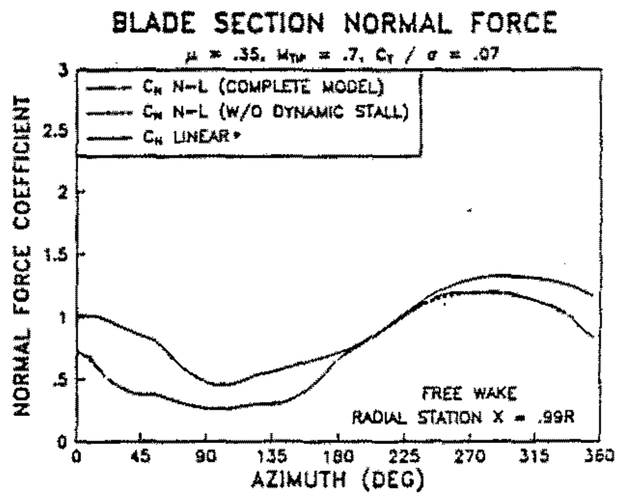

FIGURE 13.

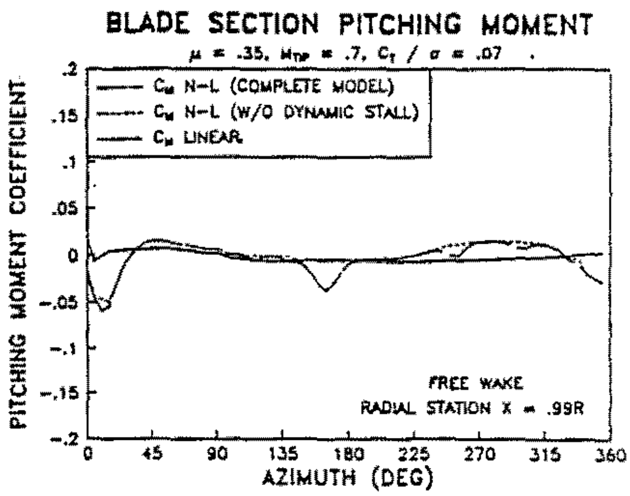

FIGURE 14.

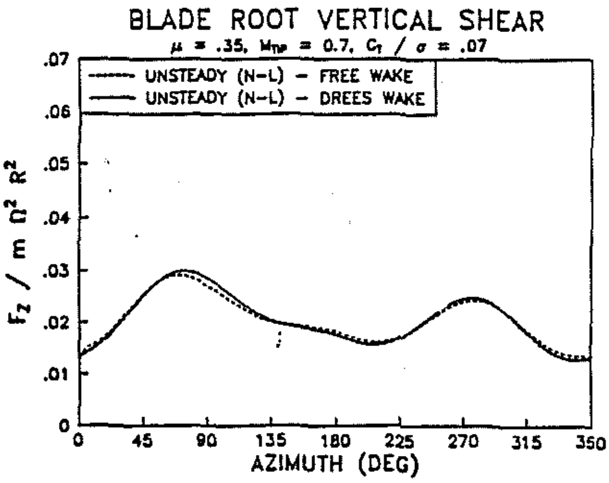

FIGURE 15.

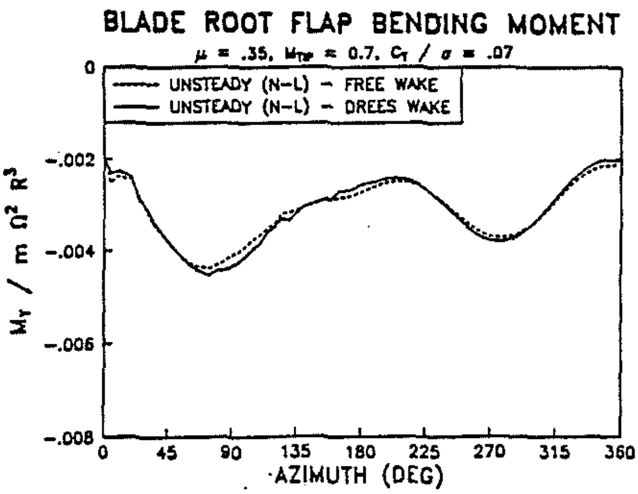

FIGURE 16.

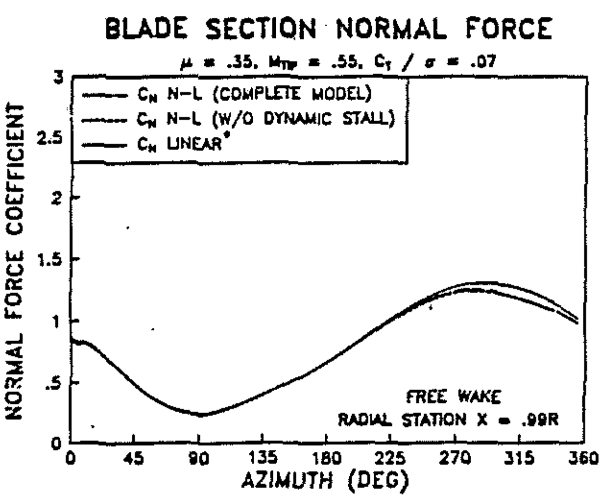

FIGURE 17.

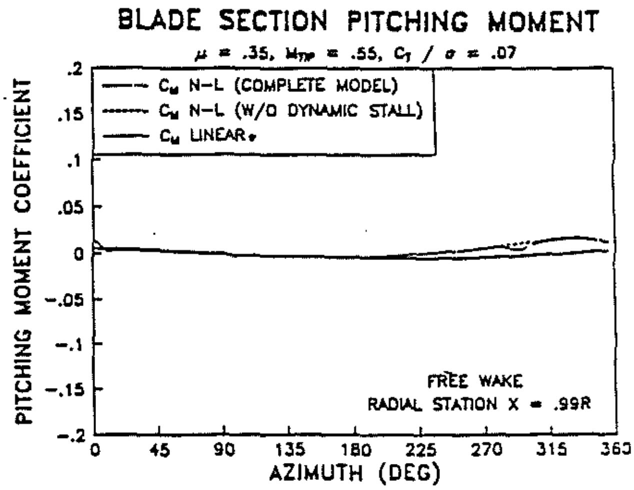

FIGURE 18.

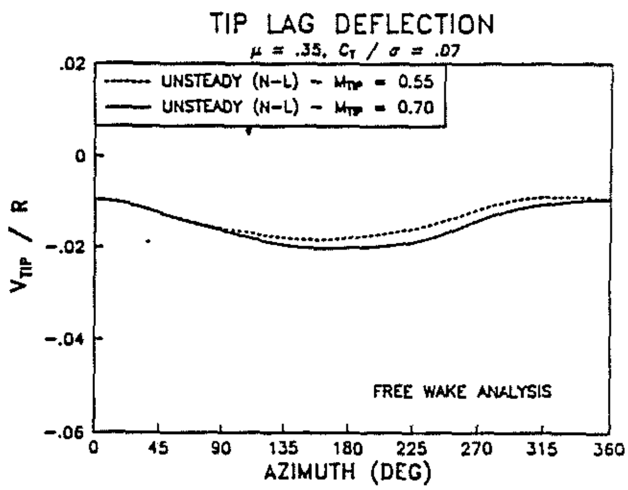

FIGURE 19.

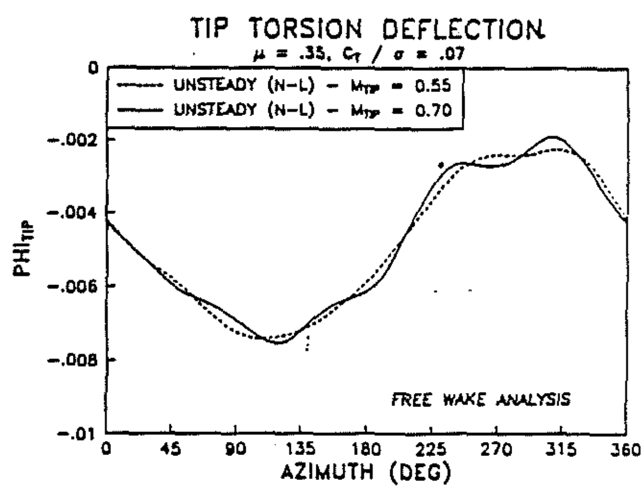

FIGURE 20.

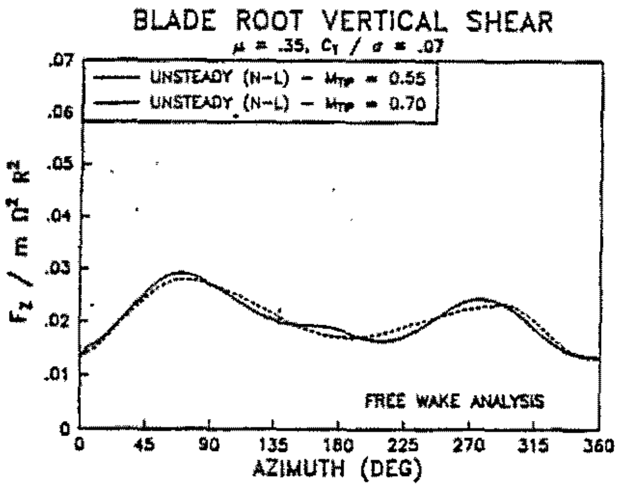

FIGURE 21.

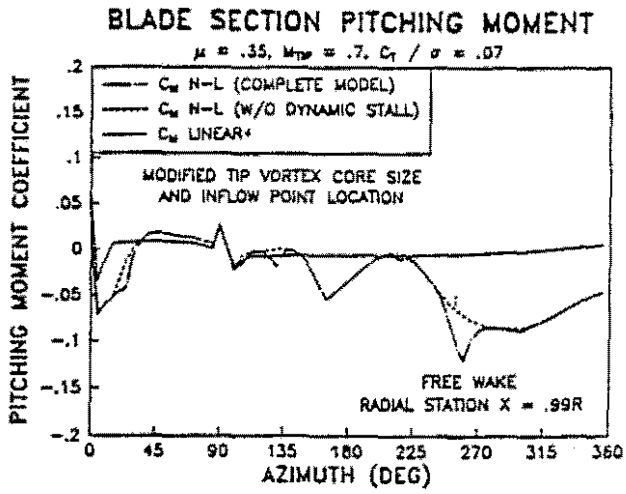

FIGURE 24.

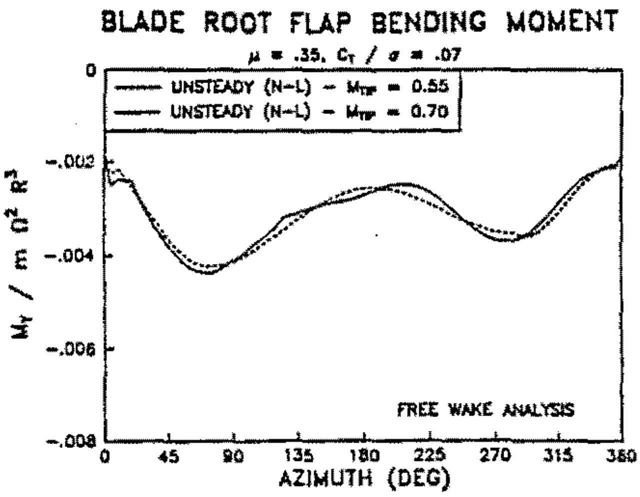

FIGURE 22.

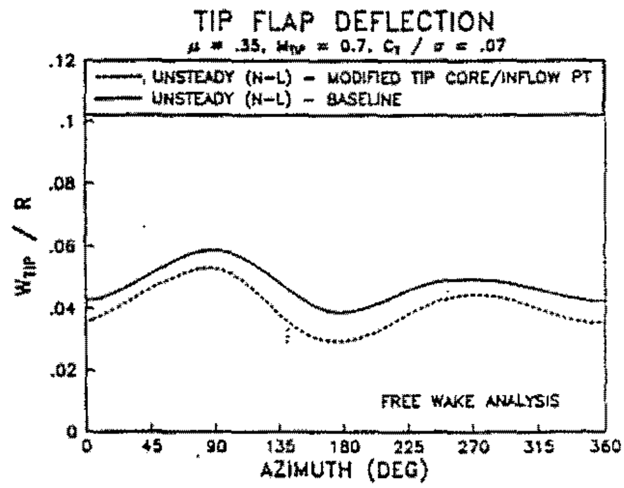

FIGURE 25.

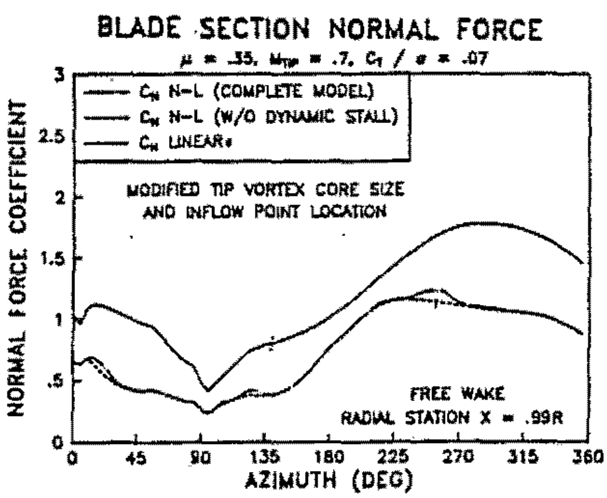

FIGURE 23.

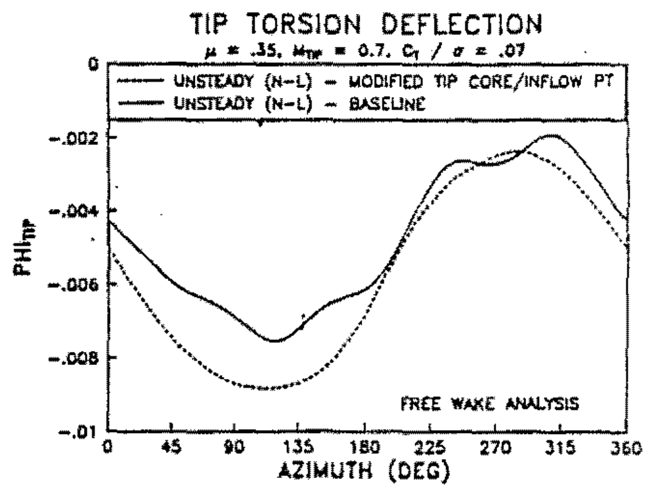

FIGURE 26.

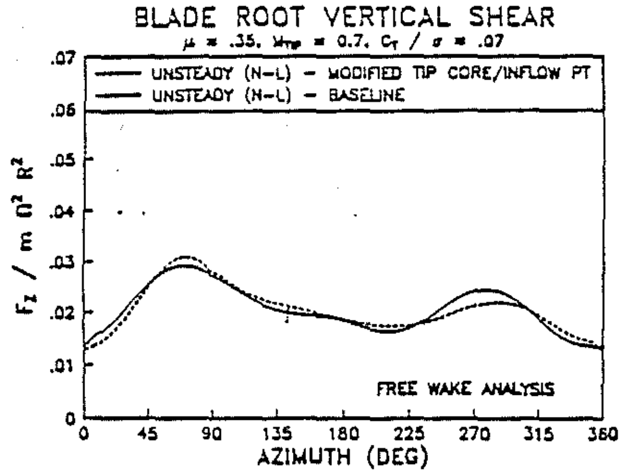

FIGURE 27.

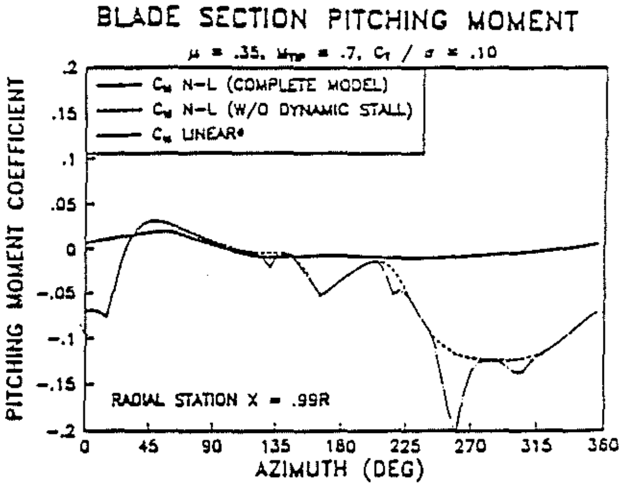

FIGURE 30.

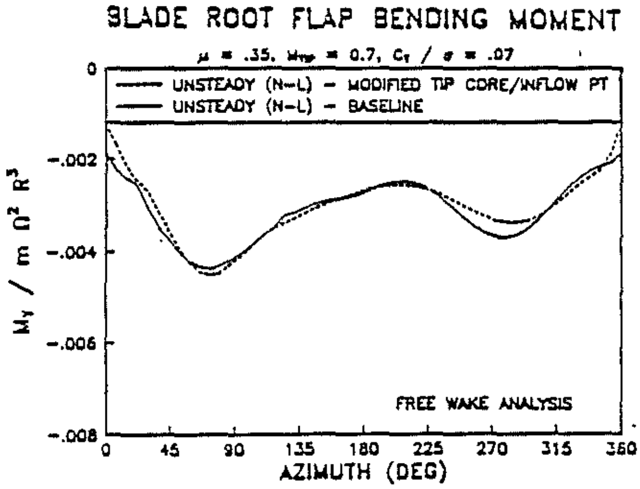

FIGURE 28.

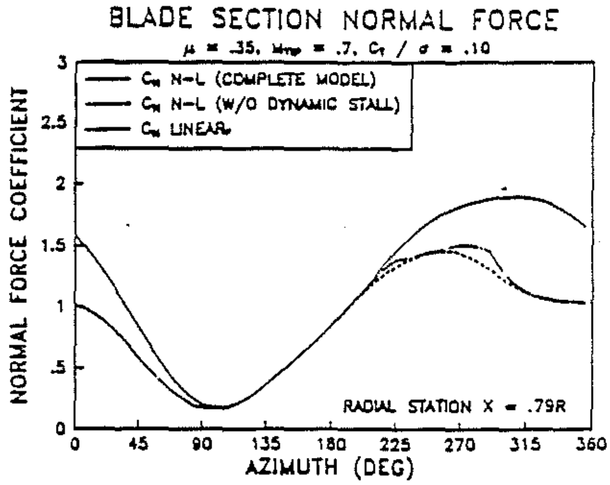

FIGURE 31.

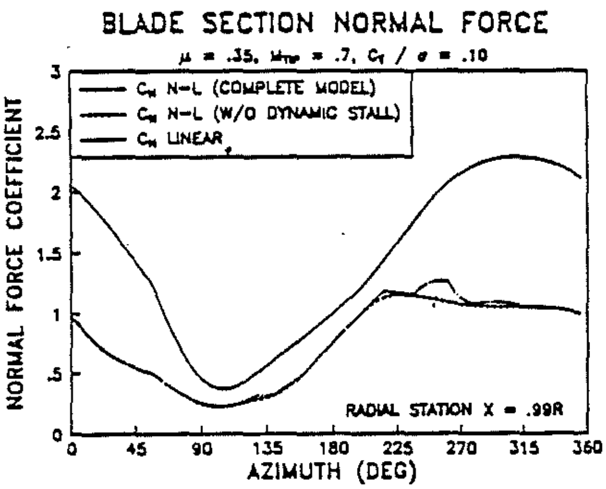

FIGURE 29.

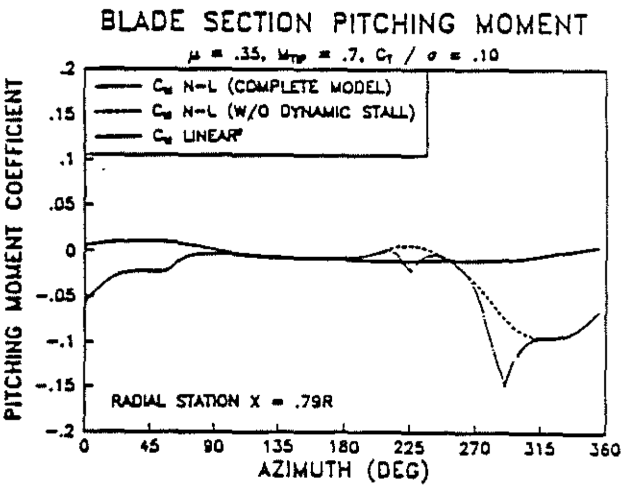

FIGURE 32.

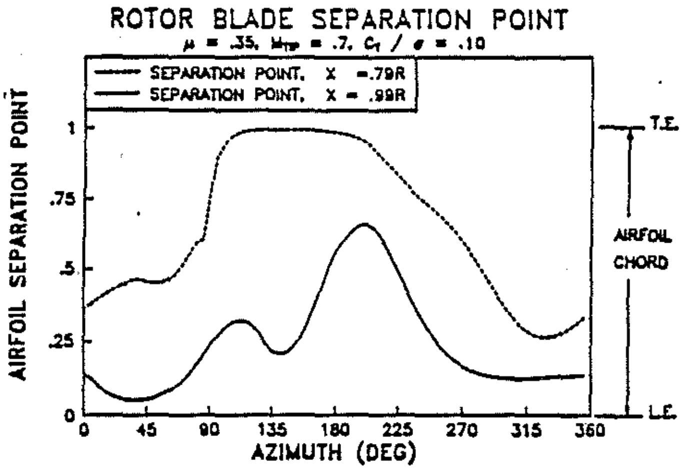

FIGURE 33.

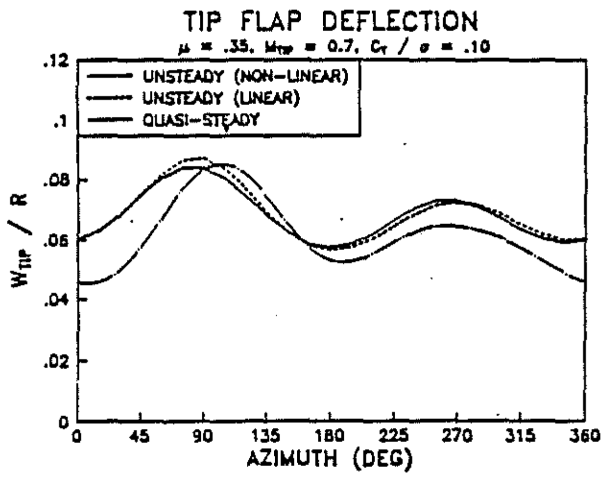

FIGURE 34.

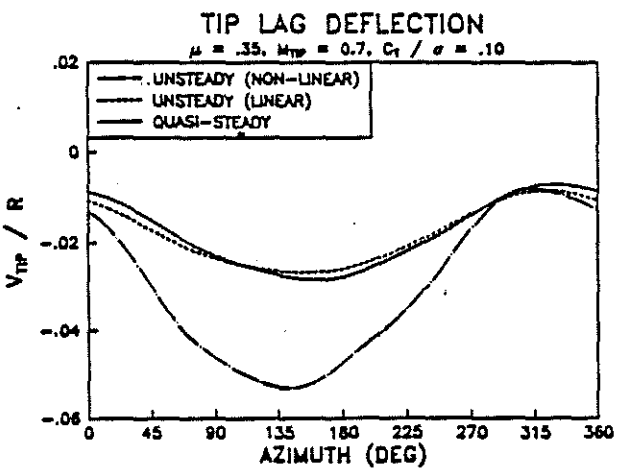

FIGURE 35.

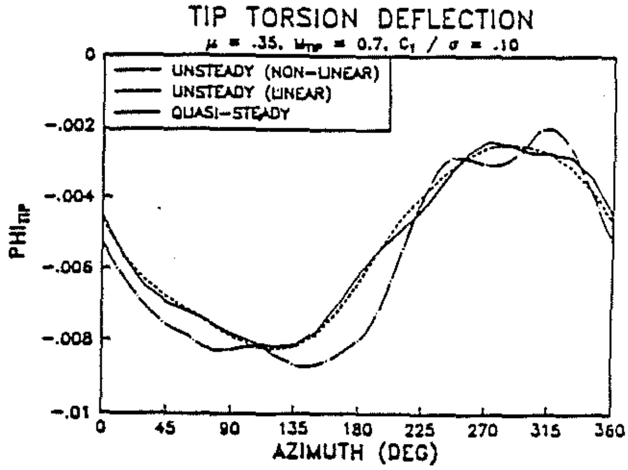

FIGURE 36.

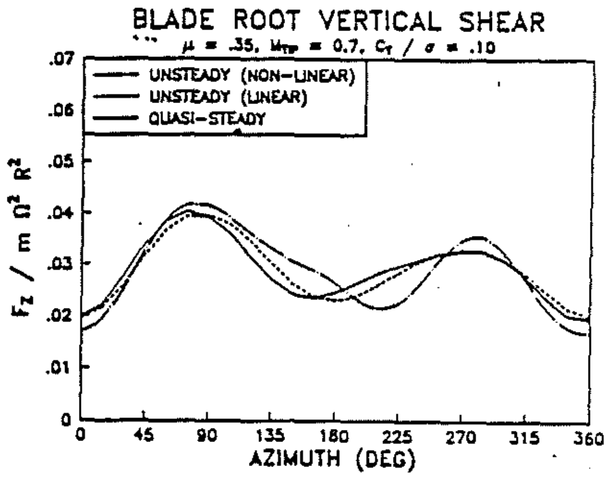

FIGURE 37.

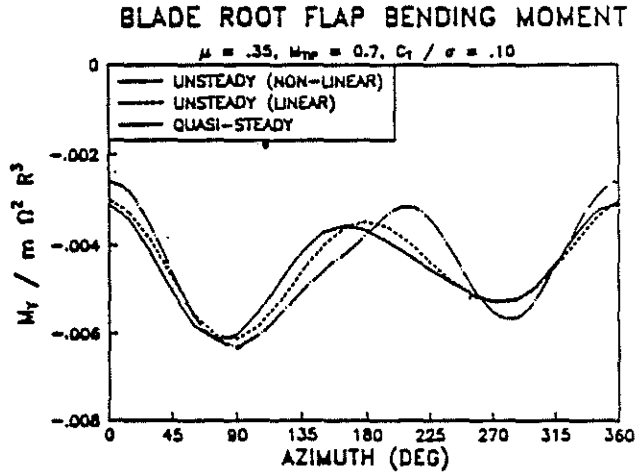

FIGURE 38.